Monthly Notices of the ROYAL ASTRONOMICAL SOCIETY

MNRAS **543,** 3214–3228 (2025) https://doi.org/10.1093/mnras/staf1676
Advance Access publication 2025 October 3

Discovery of fullerenes in the shell of candidate luminous blue variable WRAY 16-232

R. Arun [1]★ S. A. Prasoon [1,2] Blesson Mathew [2] D. Akhila [2,3] Gourav Banerjee [1] B. Shridharan [4] G. Maheswar[1] and Arun Surya[1]

[1]*Indian Institute of Astrophysics, Sarjapur Road, Koramangala, Bangalore 560034, India*
[2]*Center of Excellence in Astronomy and Astrophysics, Department of Physics and Electronics, CHRIST (Deemed to be University), Bangalore 560029, India*
[3]*Instituto de Astronomía y Ciencias Planetarias, Universidad de Atacama, Copayapu 485, Copiapó, Chile*
[4]*Tata Institute of Fundamental Research, Homi Bhabha Road, Mumbai 400005, India*

Accepted 2025 September 26. Received 2025 September 26; in original form 2025 April 28

ABSTRACT

We report the discovery of fullerene in the circumstellar environment of WRAY 16-232, a strong candidate luminous blue variable. Multiple pointings of archival *Spitzer* Infrared Spectrograph spectra reveal, for the first time, the presence of prominent vibrational bands of C_{60} at 17.4 and 18.9 μm in a luminous blue variable (LBV) envelope, along with the strong polycyclic aromatic hydrocarbon features. These observations suggest that, despite the harsh radiative conditions, large carbonaceous molecules can form, process, and survive in the ejecta of massive stars. Complementary optical spectroscopy with South African Large Telescope High-Resolution Spectrograph shows multiple P Cygni profiles in H α, He I, and Fe II lines, which are indicative of a dense, expanding wind and substantial mass-loss. Furthermore, analysis of decade long photometric data shows short-term brightness variations of ∼0.5 mag. These results not only reinforce the classification of WRAY 16-232 as a strong LBV candidate but also provide new insights into the mechanisms of dust formation and the chemical enrichment of the interstellar medium by massive stars. We discuss various scenarios for fullerene formation in such environments, and find that shock processing due to wind-wind interactions could be playing a vital role. The shell of WRAY 16-232 has an ideal UV field strength and the time-scales appear to match with shock processing time-scales. The results highlight the need for further high spatial/spectral resolution and temporal observations to confirm the formation and survival scenario of C_{60} in its shell.

Key words: astrochemistry – circumstellar matter – stars: variables: general – stars: winds, outflows – infrared: stars.

1 INTRODUCTION

Luminous blue variables (LBVs) represent a transient yet pivotal stage in the evolution of massive stars. Exhibiting dramatic photometric and spectroscopic variability (R. M. Humphreys & K. Davidson 1994), LBVs serve as a bridge between main-sequence OB stars and later evolutionary stages such as Wolf–Rayet (WR) stars or other supernova progenitors. For stars with initial masses in the range $25\,M_\odot < M < 40\,M_\odot$, the LBV phase occurs post-red supergiant evolution (J. H. Groh, G. Meynet & S. Ekström 2013), while for masses between $40\,M_\odot < M < 60\,M_\odot$, LBVs act as a precursor to the WR phase (J. H. Groh et al. 2014). Their powerful stellar winds expel CNO-processed material into the interstellar medium, thereby influencing star formation and galactic chemical enrichment (J. Puls, J. S. Vink & F. Najarro 2008; J. S. Vink 2008). The brief lifespan of the LBV phase ($\sim 10^4$–10^5 yr; R. M. Humphreys 1991) contributes to their rarity, making statistical analyses challenging. Given the small sample size of LBVs (N. D. Richardson & A. Mehner 2018), even a few misclassifications can significantly hinder our understanding of the role these objects play in massive star evolution, emphasizing the importance of applying rigorous and consistent observational criteria (R. M. Humphreys et al. 2014).

While LBVs are known for their complex circumstellar environments, the presence of fullerenes in such settings has never been reported. Fullerenes are a unique family of stable, cage-like molecules made entirely of carbon atoms, usually in even numbers. One of the most well-known and stable members of this family is buckminsterfullerene (C_{60}), commonly referred to as buckyballs. This remarkable molecule is composed of 60 carbon atoms arranged in a spherical shape, featuring 12 pentagonal and 20 hexagonal faces. C_{60} exhibits icosahedral symmetry, the highest point group symmetry for a three-dimensional molecule, making it an extremely stable and chemically resilient molecule (R. D. Johnson, G. Meijer & D. S. Bethune 1990).

Fullerenes were first identified in the laboratory by H. W. Kroto et al. (1985). The first confirmed astronomical detection of C_{60} was made by J. Cami et al. (2010) in the planetary nebula (PN) Tc 1. Since then, several studies have detected fullerenes under a range of astrophysical conditions. C_{60} has been detected in other PN (D. A. García-Hernández et al. 2010, 2012; M. Otsuka et al. 2013), in pre-main-sequence stars such as Herbig Ae/Be stars (K. R. G. Roberts,

★ E-mail: arunroyon@gmail.com

K. T. Smith & P. J. Sarre 2012; R. Arun et al. 2023), in reflection nebulae (RNe) like NGC 7023 and NGC 2023 (K. Sellgren et al. 2010), in the hydrogen-deficient and carbon-rich environments of R CrB stars (D. A. García-Hernández et al. 2011), and in post-AGB stars (V. V. Raman et al. 2017).

C_{60} formation is typically associated with the interplay of high-temperature environments and carbon-rich chemistry, but its survival in the harsh radiation fields of massive stars remains an open question (O. Berné & A. G. G. M. Tielens 2012). There are two primary formation mechanisms for C_{60} in the literature. The first is the 'top-down' process, in which large polycyclic aromatic hydrocarbon (PAH) molecules (with $N_c \geq 60$) lose their hydrogen due to UV irradiation, leading to the formation of graphenes. Continued UV exposure causes graphenes to shed C_2 units, eventually folding into closed cage structures and stabilizing as C_{60} due to their exceptional molecular stability (S. Irle et al. 2006; O. Berné, J. Montillaud & C. Joblin 2015). Also, the 'top–down' process can also occur when photochemical processing of hydrogenated amorphous carbon (HAC) grains, resulting in the formation of PAHs and fullerenes (D. A. García-Hernández et al. 2010; E. R. Micelotta et al. 2012; J. Bernard-Salas et al. 2012). The second mechanism is the 'bottom–up' process, in which small carbon-chain molecules and PAHs, subjected to UV irradiation at moderate temperatures in carbon-rich and hydrogen-poor environments (R. A. Crichton & J. Zhang 2022), assemble into fullerenes and larger PAHs, akin to laboratory synthesis methods. Beyond these linear routes, recent studies indicate a more dynamic chemical network, in which PAHs undergo fragmentation into smaller clusters (C_n, C_nH_m), which then isomerize or coalesce into cage-like structures before stabilizing as fullerenes (A. Omont & H. F. Bettinger 2021).

While several studies have reported the detection of PAHs in LBVs and WR stars (R. H. M. Voors et al. 1999; J. Rajagopal et al. 2007; F. M. Jiménez-Esteban, J. R. Meijer & A. Bethune 2010; S. V. Marchenko & A. F. J. Moffat 2017; J. R. Rizzo et al. 2023), investigations of fullerenes have predominantly focused on evolved low-mass stars (D. A. García-Hernández et al. 2012), with limited evidence for their presence in massive stars such as LBVs. To date, C_{60} has only been detected in regions where physical conditions vary over much longer time-scales, in contrast to the dynamic environments of massive stars like LBVs. These stars experience significant mass-loss and strong stellar winds during their S Doradus (S Dor) cycles, which typically span 5–10 yr and can extend beyond 20 yr (A. M. van Genderen 2001). The detection of C_{60} in the harsh and highly variable LBV environment might hint towards a potentially different formation mechanism, where C_{60} is synthesized and sustained even in the extreme conditions of LBVs.

In this study, we report the detection of C_{60} emission in *Spitzer* Infrared Spectrograph (IRS) spectra of WRAY 16-232, a previously identified candidate LBV (cLBV). Located in the constellation Ara at a distance of 2.1 ± 0.5 kpc (Gaia Collaboration 2023), WRAY 16-232 was first classified as a cLBV by V. V. Gvaramadze, A. Y. Kniazev & S. Fabrika (2010) based on archival 24 μm data from the *Spitzer*/MIPSGAL survey (S. J. Carey et al. 2009). It is designated [GKF2010] MN46, consistent with other mid-infrared (MIR) envelope sources discovered using *Spitzer*. Prior to this classification, the object had been assigned various types in the literature.

To our knowledge, WRAY 16-232 first appeared in the literature by J. D. Wray (1966), where it was initially classified as a likely PN. However, L. B. Webster (1966) later rejected this classification, and K. G. Henize (1967) labelled it as a doubtful PN. Over time, the classification of WRAY 16-232 has changed considerably. N. Sanduleak & C. B. Stephenson (1973) characterized the source as a 'very steep Balmer decrement object.' Subsequently, D. A. Allen et al. (1982) classified it as a highly obscured Be star, while D. J. MacConnell (1983) identified it as an M-type supergiant. A. Acker et al. (1992) later described it as a peculiar emission-line star. Recently, an interferometric study by L. Mahy et al. (2022) reported the presence of a companion star to WRAY 16-232 at an angular separation of 0.3 mas, corresponding to a linear separation of approximately 0.63 au (Gaia Collaboration 2023). The companion is 3.7 mag fainter than the primary star and is well within the circumstellar nebula. The circumstellar nebulae around WRAY 16-232 identified in *Spitzer* 24 μm image appears to be spherical and has a size of 0.49×0.49 pc (V. V. Gvaramadze et al. 2010; L. Mahy et al. 2022).

This paper is organized as follows: Section 2 describes the observational data, Section 3 outlines our analysis, and Sections 4 and 5 provide discussions and conclusions, respectively.

2 DATA

While compiling the *Spitzer* IRS spectra of LBVs and cLBVs listed in N. Smith et al. (2019) and L. Mahy et al. (2022), we identified WRAY 16-232 to have three distinct observations, covering the central star along with the southern and northern part of the star's envelope. This spatial configuration offers a unique opportunity to investigate the dust formation processes within the circumstellar shell of this LBV candidate. The following subsections describe the specific data sets used to study WRAY 16-232 and its surrounding envelope in detail.

2.1 *Spitzer* observations

2.1.1 Imaging

The MIR images of WRAY 16-232 were examined using archival *Spitzer* data obtained from the Infrared Processing and Analysis Center (IPAC[1]). We made use of data from the Infrared Array Camera (IRAC; G. G. Fazio et al. 2004) and the Multiband Imaging Photometer for *Spitzer* (MIPS; G. H. Rieke et al. 2004). The *Spitzer* IRAC 4 image at 8.0 μm were obtained from Galactic Legacy Infrared Mid-Plane Survey Extraordinaire (GLIMPSE; R. A. Benjamin et al. 2003) survey and the MIPS1 image at 24 μm were obtained from Multiband Imaging Photometer for Spitzer Galactic Plane Survey (MIPSGAL: S. J. Carey et al. 2009). The IRAC 4 data have higher-resolution (∼2 arcsec) than MIPS 1 (∼6 arcsec) data. All *Spitzer* data were retrieved as pipeline-processed mosaic products.

2.1.2 Spectroscopy

The MIR spectra of WRAY 16-232 were retrieved from the Combined Atlas of Sources with *Spitzer* IRS Spectra (CASSIS[2]) archive (V. Lebouteiller et al. 2011, 2015). The spectra were obtained as part of the *Spitzer* programme titled 'IRS Investigation of 24 Micron Compact Ring Sources' (Programme ID: 50808, PI: Sean Carey). Observations were carried out on 2009-04-21 at 04:47:53 UTC and

[1]https://www.ipac.caltech.edu/doi/irsa/10.26131/IRSA433. IPAC is hosted by California Institute of Technology (Caltech) and operates under contract with National Aeronautics and Space Administration (NASA).
[2]CASSIS is a product of the IRS instrument team, supported by NASA and JPL.

are identified by the Astronomical Observation Request (AOR) Key 32555008.

The data set includes three distinct pointings, separated by 0.79 arcsec (centre), 44.13 arcsec (north), and 47.34 arcsec (south) from the central target. The spectra were acquired using the low-resolution (LR) mode of the IRS instrument, covering the wavelength range of 7.8–35 μm. The 6–7.5 μm region was not observed in this programme.

The raw spectra were processed using the enhanced offline pipeline CASSISjuice (V. Lebouteiller 2023). CASSISjuice improves data usability by organizing pointings under a unified target ID and incorporating a robust and consistent pipeline for all IRS staring-mode observations.

2.2 SALT HRS spectroscopy

The optical spectra analysed in this study were obtained from the South African Large Telescope (SALT) High-Resolution Spectrograph (HRS; S. I. Barnes et al. 2008; D. G. Bramall et al. 2010, 2012; L. A. Crause et al. 2014) archive. The data were taken on 2016-05-16 using the HRS in its low-resolution mode, which provides a resolving power of $R \sim 16\,000$ with a exposure time of 2400 s (Prop ID: 2016-1-SCI-012 - PI: Alexei Kniazev). It is important to note that seven spectra of WRAY 16-232, spanning a period of 7 yr (2022 May 2016 to September), are available in the SALT archive. For the detailed line analysis, we use the observation closest in time to the *Spitzer* observation. Since the primary aim of this article is to report the discovery of fullerenes in WRAY 16-232, we did not undertake a comprehensive multi-epoch analysis. Nevertheless, we performed a preliminary investigation of the Hα line to assess the variable nature of WRAY 16-232.

The reduced data of WRAY 16-232 is taken from the SALT archive.[3] The primary reduction such as overscan correction, bias subtractions and gain correction, was carried out with the SALT science pipeline (S. M. Crawford et al. 2010). And the spectroscopic reduction of the HRS spectra is reduced using the MIDAS pipeline (A. Y. Kniazev, V. V. Gvaramadze & L. N. Berdnikov 2016; A. Y. Kniazev, V. V. Gvaramadze & L. N. Berdnikov 2017), which includes standard procedures such as bias subtraction, flat-fielding, wavelength calibration, and cosmic ray removal. These archival reductions ensured that the spectra were ready for scientific analysis, removing the need for additional data processing. Due to the very low signal-to-noise ratio in the blue arm (3900–5500 Å), these data were excluded from the analysis. Our study is therefore based on the red arm spectra, covering the 5400–8900 Å range.

2.3 Photometry

To study the photometric variability, we compiled the available magnitudes for WRAY 16-232.The photometric magnitudes, along with stellar parameters of the star is mentioned in Table 1. There are significant difference between the *B*- and *R*-band magnitudes, with the *B* band being 4.2 times dimmer than the *R* band, indicating high extinction towards the star.

To investigate the photometric variability of WRAY 16-232, we retrieved *Gaia G*-band, *BP*-band, and *RP*-band photometric data (Gaia Collaboration 2016, 2023), spanning from October 2014 to March 2017. Additionally, *V*-band photometric data were obtained from the All-Sky Automated Survey for Supernovae (ASAS-SN; B. J. Shappee et al. 2014; T. Jayasinghe et al. 2019), observed between March 2016 and October 2018 (C. S. Kochanek et al. 2017). Notably, a brightening event is evident in both the *Gaia G*-band and *ASAS-SN V*-band light curves between January 2017 and March 2017. We also incorporate *r*-band and *i*-band photometry from the Bochum Galactic Disk Survey (GDS), as presented in M. Hackstein et al. (2015). It provides time-series observations of the Southern Galactic plane. The *r*- and *i*-band magnitudes of WRAY16−232 span from 2014 May 2011 to August.

Table 1. Photometric and positional properties of WRAY 16-232. Photometric magnitudes are obtained from V. V. Gvaramadze et al. (2010), whereas the distance is taken from the Gaia Collaboration et al. (2023).

Property	Value
RA (h:m:s)	16:43:16
Dec. (d:m:s)	−46:00:42
distance (kpc)	2.1 ± 0.5
B band	17.12
V band	15.66
R band	12.92
J band	6.26
H band	5.08
K band	4.21

3 ANALYSIS AND RESULTS

3.1 Study of the *Spitzer* IRAC/MIPS images

The *Spitzer* IRAC 4 and MIPS 1 images show the envelope around WRAY 16-232, which is shown in Fig. 1. The MIPS 1 image in the right panel of Fig. 1 reveals a nearly spherical envelope around the star. The nebulae surrounding LBVs can be bipolar, spherical, or irregular; for example, a spherical shell has been reported around the LBV source S119 (K. Weis, W. J. Duschl & D. J. Bomans 2003). The spherical shell of WRAY 16-232 is illustrated in V. V. Gvaramadze et al. (2010), although its internal features were not examined in detail in that study. Based on the MIPS 1 image, we estimate the envelope to have a radius of 1.2 arcmin, corresponding to 0.70 pc. This falls well within the typical range of LBV dust shell radii, which often span from 0.1 to 2 pc (K. Weis & D. J. Bomans 2020). This shell appears relatively bright and well-defined, suggesting a concentration of dust that is being heated by the central source and re-radiating strongly at 24 μm. Several brighter arcs or knots of emission trace out an inhomogeneous distribution of material, implying that the dust is clumpy or shaped by localized outflows and wind–wind interactions of faster and slower winds during a S Dor cycle (A. Nota 1999). The extended tail-like structure observed toward the south does not appear to be part of the spherical shell, but rather belongs to a larger, more diffuse region, as confirmed through visual inspection.

The IRAC 4 image has a higher resolution than MIPS 1 and they highlight the clumpy and arc-like denser structures. The 8 μm image shows warmer dust and potentially traces regions more influenced by PAH emission (L. Deharveng et al. 2010; R. Arun et al. 2021), within the main shell. These regions may mark zones where dust composition or temperature differs from the shell's dominant 24 μm emission. The arc-like structures appear to converge or point toward the central star, suggesting they may be shaped by directed outflows or strong stellar winds. The 'heads' of these structures likely trace regions of denser dust that have been compressed or sculpted by these

[3] https://ssda.saao.ac.za/

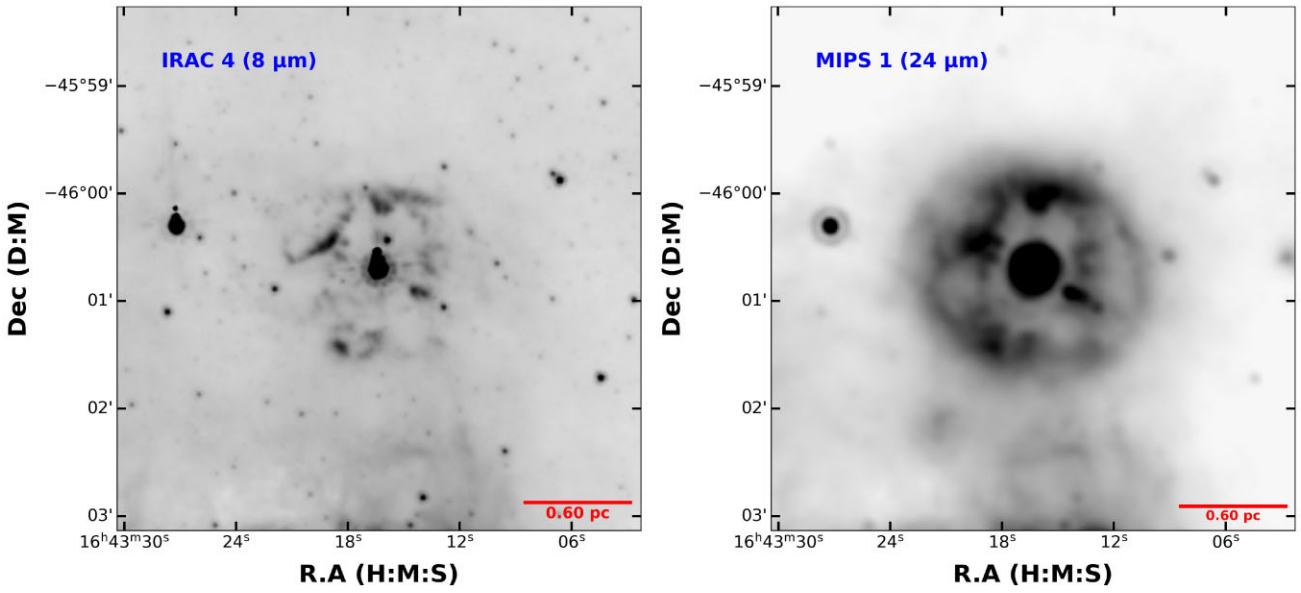

Figure 1. Infrared images of WRAY 16-232 showcasing its circumstellar environment. Left: *Spitzer* IRAC 4 (8 μm) image highlighting the distribution of PAHs and warm dust in the nebula. Right: *Spitzer* MIPS 1 24 μm image emphasizing thermal emission from cooler dust grains in the circumstellar shell. Both images are oriented with north up and west to the left. The nebula exhibits a nearly spherical morphology, traced by the 24 μm cool dust, with clumpy structures and arc-like features more pronounced in 8 μm, suggesting complex mass-loss processes and wind interactions.

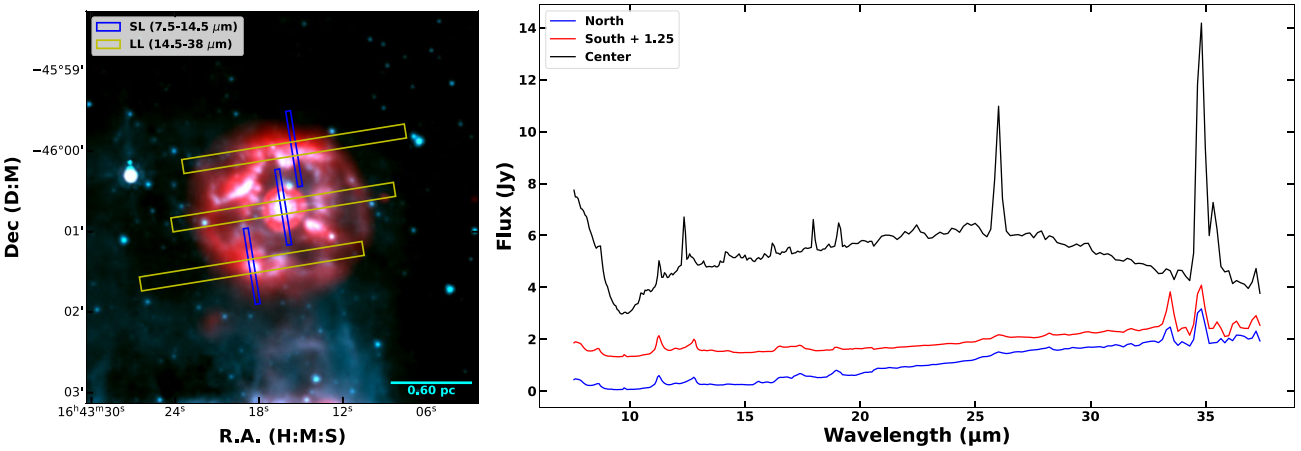

Figure 2. Left: *Spitzer* IRAC MIPS false colour image [8 μm (IRAC 4) – turquoise and 24 μm (MIPS 1) – red] is shown with slit orientation of three pointing from *Spitzer* IRS Short Low (SL) and Short High (SH). Right: *Spitzer* IRS spectrum of the three regions. The south pointing flux is increased for visibility of the figure.

forces. The IRAC 4 image shows a more concentrated emission in the head structure, indicating the presence or formation of PAHs at an inner radius <0.7 pc. Overall, the image data depict a rich, layered envelope whose morphology appears to be shaped by multiple mass-loss episodes and complex wind dynamics associated with an evolved massive star. These characteristics offer insights into the star's LBV nature.

3.2 MIR spectral properties of WRAY 16-232 and comparison with other LBVs

Continuum subtraction for the LR ($R \sim 60$) spectra of WRAY 16-232–covering the central source and two envelope positions to the north and south (Fig. 2) was performed using a spline-fitting method similar to that employed by J. Y. Seok & A. Li (2017) and R. Arun et al. (2023). Anchor points were selected in the 7–36 μm range, avoiding strong emission lines and PAH features and were modelled separately for the central and envelope spectra. For the central source, anchor points were placed at 7.6, 8.0, 8.3, 9.25, 10.3, 11.7, 13.0, 13.7, 13.9, 14.1, 14.4, 14.6, 15.35, 16.0, 18.3, 19.8, 20.3, 21.5, 23.4, 27.0, 28.5, 30.0, 32.0, 33.0, 34.1, 36.1, and 36.8 μm, while for the northern and southern envelopes, they were set at 7.6, 8.0, 8.1, 9.25, 10.3, 11.7, 13.1, 14.5, 15.35, 16.2, 18.3, 19.8, 20.0, 22.0, 24.0, 28.0, 30.0, 32.0, 33.0, 33.8, 35.2, and 36.5 μm. A cubic spline fit to these points modelled the continuum, which was then subtracted to isolate emission features. The continuum-subtracted spectra, which is shown in Fig. 3, exhibit distinct variations across the three pointings, particularly in continuum morphology and emission features. The key similarities and differences are summarized below and further analysed in the context of MIR spectral characteristics of other known LBVs.

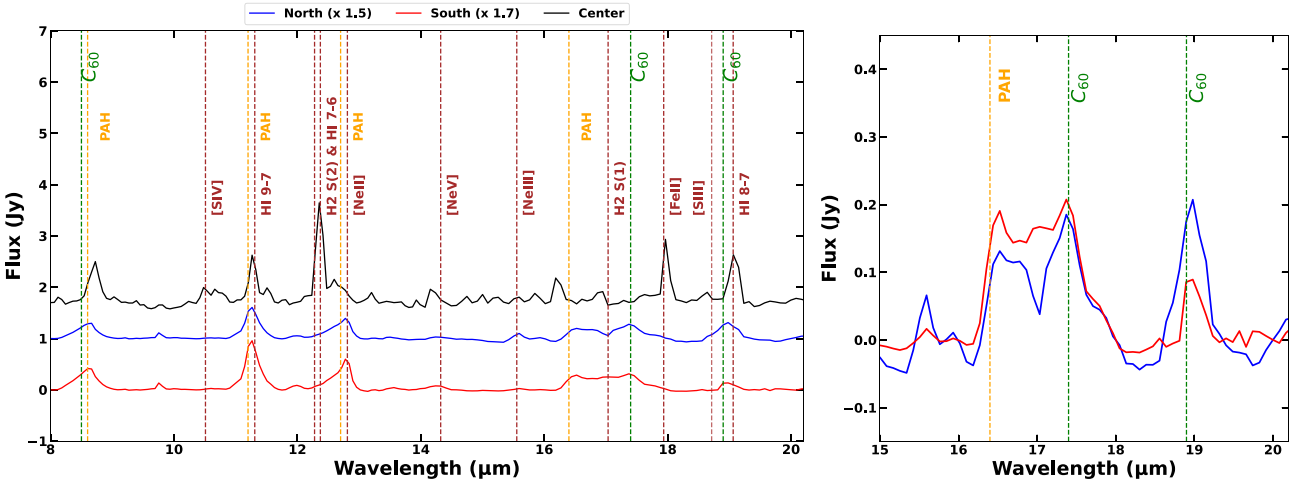

Figure 3. Continuum-subtracted *Spitzer*/IRS spectra of the centre, north, and south regions of WRAY 16-232 (left), offset vertically for clarity. Vertical dashed lines mark prominent emission lines and PAH/fullerene features, with labels denoting their identifications. Each spectrum is scaled as indicated in the legend to highlight variations in line strengths among the regions. The zoomed-in region shows the 17.4 and 18.9 μm C_{60} features identified in the northern and southern parts of the envelope (right).

(i) Dust Continuum and Silicate Absorption**:** The spectrum corresponding to the central pointing is characterized by a rising continuum beyond the silicate absorption feature at 9.7 μm. This is similar to what is observed in the Galactic cLBV G79.29+0.46 (F. M. Jiménez-Esteban et al. 2010). The absorption points to optically thick and cooler dust temperatures in the line of sight. An A_V value of 12 mag measured using the optical depth of 9.7 μm silicate absorption for WRAY 16-232 supports an optically thick line of sight (M. Nowak et al. 2014). In contrast, this silicate feature appears in emission in many other LBVs, such as HR Car (G. Umana et al. 2009), HD 168625 (G. Umana et al. 2010) and WRA 751 (R. H. M. Voors et al. 2000).

Interestingly, the envelope spectra of WRAY 16-232 show flatter mid-IR continua and weak or absent silicate absorption, suggesting either reduced silicate dust or different excitation conditions farther from the central star. Notably, the northern envelope slope beyond 15 μm is steeper than the southern one, which may reflect variations in dust column density or temperature along different viewing directions.

(ii) Ionized and Atomic Fine-Structure Lines: In the central pointing, we detect a range of ionic lines, such as those of [Si II] 34.83 μm and [Fe II] transitions at 17.96, 25.99, and 35.35 μm. These lines are characteristic of the presence of some hot, ionized environments, associated with massive stars having strong UV fields. Similar fine-structure lines are also observed in the MIR spectra of known LBVs (G. Umana et al. 2010) e.g. HR Car (G. Umana et al. 2009), alongside strong free–free or dust emission. The envelope spectra also feature some faint lines such as [Ne III] 15.55 μm, [Fe II] 25.99 μm, and [S III] 33.49 μm. This reduction in line strength is likely due to decreased excitation or density with increasing distance from the central star.

(iii) Hydrogen Recombination and Helium Lines: Hydrogen recombination lines (e.g. H I at 8.76, 12.37, 16.88, 19.06, 27.8 μm) and He II lines (10.47, 13.13, 22.18 μm) are detected across all three pointings, with the strongest and most numerous features observed in the central source. Strong hydrogenic emission lines are a key mid-IR signature of massive stars with substantial ionizing radiation (W. L. F. Marcolino et al. 2017). Similar features have been identified in LBVs such as P Cygni and AG Car, often accompanied by prominent P Cygni profiles in the optical or near-IR (F. Najarro, D. J. Hillier & O. Stahl 1997). Their detection in both the stars and its surrounding envelope suggests the presence of an extended ionized region shaped by strong stellar winds.

(iv) Molecular Hydrogen and PAHs: Both envelope pointings exhibit H_2 rotational lines, including S(0) at 28.22 μm and S(3) at 9.66 μm. Additionally, the S(2) line at 12.28 μm is detected in the spectrum of the central object. Pure rotational lines of H_2 have been identified in only a few LBVs, such as the candidate LBVs HDE 316285 (P. Morris, P. W. Morris & Spitzer WRRINGS Team 2008) and G79.29+0.46 (F. M. Jiménez-Esteban et al. 2010). Alongside the H_2 lines, we also report the detection of prominent PAH bands at 8.6, 11.2, 12.7, and possibly 16.4 μm, consistent with previous detections in other LBVs and cLBVs (C. J. Skinner 1997; R. H. M. Voors et al. 1999, 2000).

The strong PAH emission in the envelopes of WRAY 16-232 suggests the presence of carbon-rich ejecta, likely processed in the extended dust shell, possibly a remnant of earlier mass-loss episodes. Additionally, the presence of 16.4 μm and 17.4 μm PAH features, later found to be contaminated by C_{60} and attributed to larger PAHs containing 50–130 carbon atoms, has not been previously reported in evolved stars and LBVs (C. Boersma et al. 2010). Their presence indicate that the envelope around WRAY 16-232 has optimal environment for forming larger PAH molecules. In contrast, the absence or suppression of PAH features along the line of sight toward the central star may be attributed to a hotter dust environment or silicate-dominated material, which does not efficiently form the PAHs.

(v) Fullerene Signatures: As shown in the right panel of Fig. 3, the envelope spectra of WRAY 16-232 reveal distinct C_{60} features at 17.4 and 18.9 μm, whereas we did not notice these lines in the central source. This marks the first reported detection of fullerenes in a cLBV envelope, given that fullerene emission in high-mass star ejecta has not been reported to date and has, thus far, been more commonly observed in PN (e.g. J. Cami et al. 2010; D. A. García-Hernández et al. 2012). Since LBVs undergo episodic mass-loss and dust formation in harsh radiative environments, the presence of C_{60} in WRAY 16-232 provides a unique window into carbon processing under intense UV fields. The 16.4 μm PAH emission is

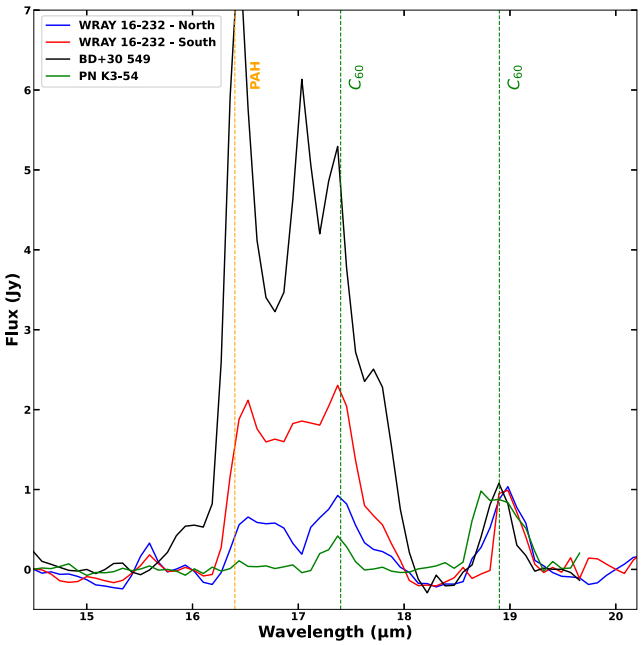

Figure 4. Continuum-subtracted *Spitzer*/IRS spectra of WRAY 16-232 (north and south), BD+30 549 (RNe), and PN K3-54, normalized to unity at the 18.9 μm C_{60} feature. The 17.4 and 18.9 μm fullerene bands are detected in all sources, but their relative strengths vary depending on the physical conditions of the local environment.

notably stronger in the southern spectrum, and the 17.4 μm feature also shows enhanced intensity there, indicating that the feature has a PAH contribution along with the fullerene as mentioned in the literature.

The mid-IR spectral properties of WRAY 16-232 exhibit key LBV characteristics, including a strong dust continuum, presence of fine-structure lines [Fe II], [Ne III], and [S III] typical of ionized nebulae, and a chemically diverse circumstellar environment. The combination of silicate absorption in the central source with PAH and fullerene emission in the envelope points to a complex, multistage mass-loss history, potentially influenced by episodic ejections at different evolutionary phases or binarity. The detection of C_{60} further highlights the role of UV-driven processes in shaping the circumstellar medium. These findings suggest that WRAY 16-232 is an evolved massive star undergoing active dust processing, with its intricate chemical composition and mass-loss patterns warranting further investigation.

3.3 Comparison with other C_{60} sources

We compare the continuum-subtracted spectra of WRAY 16-232 (north and south regions) with two well-known fullerene-rich sources: BD+30 549, a RNe and PN K3-54 (M. Otsuka et al. 2013; R. Arun et al. 2023) in Fig. 4. All spectra are normalized to unity at the 18.9 μm C_{60} feature to facilitate direct comparison.

The 16.4 μm PAH emission varies significantly among the sources. BD+30 549, which is associated with a RNe known for strong PAH emission, exhibits an enhanced 16.4 μm PAH feature along with a higher level of PAH contamination in the 17.4 μm region. In contrast, the PN K3-54 spectrum is nearly devoid of PAH emission, showing only the pure C_{60} features at 17.4 and 18.9 μm. Notably, in the PN spectrum, the 17.4 μm feature is significantly weaker than the 18.9 μm feature, which is characteristic of a fullerene-dominated environment (D. A. García-Hernández et al. 2010).

WRAY 16-232 presents an intermediate spectrum between these two extremes. While PAH emission is evident, particularly in the southern envelope, the 16.4 μm PAH feature is not as intense as in BD+30 549, suggesting a less PAH-rich environment. However, the relative intensity of the 17.4 μm feature is elevated in the south, indicating that PAH contamination is contributing to this band, unlike in PN K3-54, where the 17.4 μm feature is purely due to C_{60}. This suggests that fullerene formation in WRAY 16-232 occurs in an environment with active PAH processing, distinguishing it from the more chemically evolved PN K3-54, where PAHs are largely absent. The comparison highlights how LBV ejecta can provide conditions for fullerene formation that are distinct from both RNe and PN.

3.4 Analysis of SALT HRS spectra

By analysing the SALT HRS spectra of WRAY 16-232, we identified a total of 109 emission lines, with P Cygni morphology being the most prevalent. This indicates the presence of an expanding circumstellar shell and substantial mass-loss from the star (J. A. Rottenberg 1952). Additionally, the near absence of stellar photospheric absorption lines suggests that the spectral continuum is primarily dominated by stellar winds.

The Hα line exhibits a P Cygni profile (Fig. 5) with very broad wings, indicative of regions with significant electron scattering (A. P. Bernat & D. L. Lambert 1978). In case of classical Be stars, the Hα line normally does not show the P Cygni profile regardless of the environment (T. Rivinius, Carciofi & Martayan 2013; G. Banerjee et al. 2022) which completely rules out the SIMBAD classification of WRAY 16-232 as a Be star. Additionally, all Paschen series lines display P Cygni profiles. Weak P Cygni profiles are observed in He I $\lambda\lambda$5876, 6679, 7065, and 8582, characterized by very broad absorption components that are significantly shifted from their rest wavelengths, suggesting the presence of a high-velocity region. The spectrum also features a forest of Fe II lines, some appearing in pure emission and others with P Cygni profiles. Prominent Fe II P Cygni lines include $\lambda\lambda$6149, 6456, and 7711. Additionally, three [Fe II] forbidden lines were detected.

The analysis of the HRS spectra reveals the presence of singly ionized lines of N II, Si II, Al II, Ca II, and Mg II. Among these, the detected Ca II lines include the well-known Ca II triplet ($\lambda\lambda$8498, 8542, 8662), which is blended with Paschen lines (P16, P15, and P13, respectively). The presence of the Ca II triplet suggests a cooler region ($T \sim 5000$ K; Y. Chmielewski 2000) within the circumstellar environment. Additionally, several N I lines were identified, which are characteristic features commonly observed in many LBVs (K. Davidson, N. R. Walborn & T. R. Gull 1982). O I lines, including the triplet at λ7775 and λ8446 (blended with an Fe II line), were also detected.

Moreover, several fine-structure lines are identified in the HRS spectra of WRAY 16-232 as well. These include multiple [Fe II] lines, which are typical features of LBVs, as well as the [N II] $\lambda\lambda$5755 and 6584 nebular lines. The [N II] λ6584 line is superimposed on the broad emission wings of Hα. The [N II] line also appears to be blended with the C II 6582 feature, which is commonly observed in other LBVs, like P Cygni. The [Fe II] λ7155 and [N II] λ5755 lines, if exhibiting flat-topped profiles, could potentially be used to calculate the terminal velocity (v_∞; O. Stahl et al. 1991). No such line structures were observed in the spectra, precluding direct velocity measurement. Nevertheless, by tracing the blue edge of the absorption components, an upper limit for the terminal velocity was

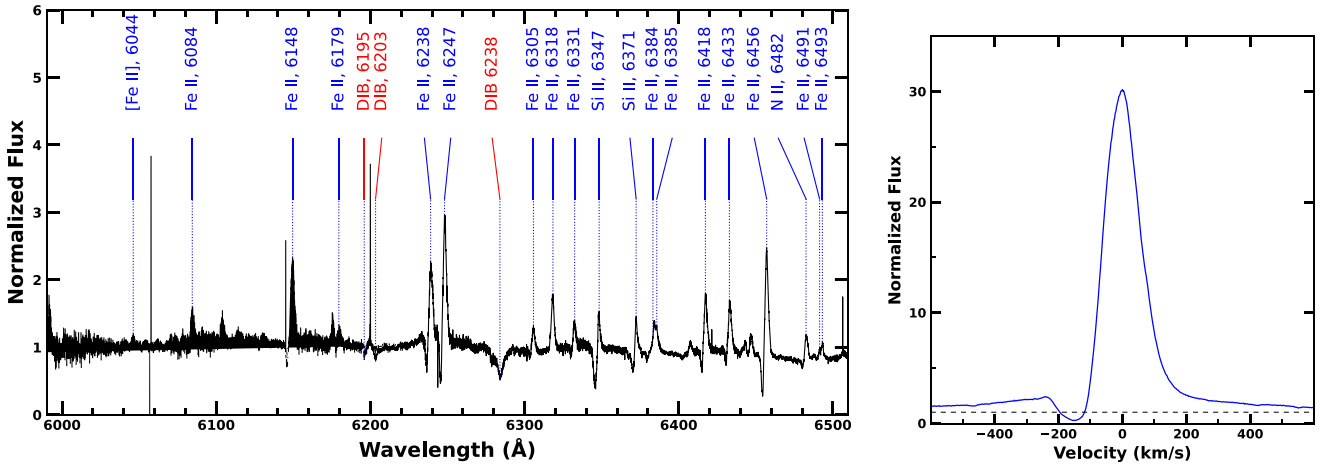

Figure 5. Portion of SALT HRS spectra of WRAY 16-232 in the left panel (obtained on 16 May 2016). The thin lines in the region are likely caused by cosmic ray hits or instrumental artefacts. The right panel depicts the H α line in WRAY 16-232, where the blue edge of the absorption component roughly indicates the terminal velocity.

estimated to be $v_\infty \approx 244$ km s^{-1}. This method has also been widely adopted by other authors, for example, A. Y. Kniazev et al. (2016). Our estimated v_∞ closely matches that of the prototype Galactic LBV AG Car during its quiescent phase, which was reported by J. H. Groh et al. (2009) to be 270 ± 50 km s^{-1}. This similarity suggests that WRAY 16-232 was likely in a quiescent phase at the time spectra were obtained, i.e. during May 2016. It is also worth noting that a lower terminal velocity of 225 km s^{-1} was estimated by O. Stahl et al. (2001) during AG Car's visual minimum phase, although they acknowledged that their estimate, based on a β-law velocity profile, likely underestimates the true terminal velocity. To better contextualise the v_∞ value of WRAY 16-232, the terminal wind velocities of other LBVs in their quiescent phases are as follows: P Cygni – 310 km s^{-1} (H. J. G. L. M. Lamers, P. Korevaar & A. Cassatella 1985), HD 168625-350 $\pm$ 100 km s^{-1} (L. Mahy et al. 2016), Romano's Star – 265 km s^{-1} (J. S. Clark et al. 2012), and [GKF 2010] MN48-152 $\pm$ 5 km s^{-1} (A. Y. Kniazev et al. 2016). A v_∞ of approximately 244 km s^{-1} is consistent with the observation that LBV winds are slower compared to those of other supergiants (J. S. Vink 2018b). The right panel in Fig. 5 illustrates the H α line in the WRAY 16-232 spectrum.

Numerous diffuse interstellar bands (DIBs) were observed in the spectrum, including $\lambda\lambda$5780, 5797, 5849, blended 6195 and 6196, 6203, 6613, 6660, 6699, 6729, 8621, and a broad, blended feature spanning $\lambda\lambda$6276–6288. The identification of DIBs in our spectra was made by comparing with the features reported in P. Jenniskens & F. X. Desert (1994), K. Słyk et al. (2006), and K.-F. Wu et al. (2022). Additionally, a broad interstellar absorption band corresponding to Na D1 and D2 is present.

Measuring the extinction parameter (A_V) using the strength of DIBs is a common approach employed in numerous studies (A. S. Carvalho & L. A. Hillenbrand 2022; S. Nidhi et al. 2023; X.-X. Ma et al. 2024). We calculated the A_V using the DIB strength of the 6613 Å line. The equivalent width (EW) of the DIB was related to the reddening value $E(B-V)$ using the equation:

$$E(B-V) = a + b \cdot \mathrm{EW}_{\mathrm{DIB}}, \quad (1)$$

where the coefficients $a = 1.96 \times 10^{-2}$ and $b = 4.63 \times 10^{-3}$. The Equation 1 is adopted from S. D. Friedman et al. (2010). The extinction, $A_V = R_V \cdot E(B-V)$, assuming an total-to-selective extinction of $R_V = 3.1$ (for the Milky Way) we determined $A_V = 0.0664$. The DIB based A_V values are only reliable for measuring interstellar (line-of-sight) extinction, but they do not account for extinction caused by the envelope around an LBV (V. G. Klochkova, E. S. Islentieva & V. E. Panchuk 2022). One other caveat is that the galactic R_V value would change for such environments due to the envelope in the line of sight, as indicated by the silicate absorption. For example, in the case of LBV HR Car, the measured R_V is 4.3 ± 0.1, indicating much larger grain sizes in its circumstellar environment compared to the average interstellar value (A. Mehner et al. 2021). Hence, in order to resolve the ambiguity, we have adopted the A_V from M. Nowak et al. (2014) for the present study.

P. Massey, E. Waterhouse & K. DeGioia-Eastwood (2000) and references therein argued that the presence of a dense forest of [Fe II] lines indicates that the LBV is in its visual minimum state, during which the temperature of LBVs ranges from approximately 12 000 to 30 000 K (T. Kogure & K.-C. Leung 2007). In the optical spectra of WRAY 16-232, we observe a few [Fe II] lines, though not a dense forest. In contrast, there is a prominent forest of Fe II lines. Coupled with the absence of higher ionization features such as Fe III, this suggests the presence of relatively low-temperature regions in the vicinity of WRAY 16-232. Fe III lines are generally expected during visual minimum or quiescent phases, when LBV temperatures are high (12 000–30 000 K). Their absence may be due to the high optical depth reported by M. Nowak et al. (2014), which could have obscured these lines.

LBVs can exhibit episodic mass-loss, leading to variations in wind velocity at different distances from the central star. A common spectroscopic method for determining LBV wind velocities involves using the Doppler shift formula.

We computed wind velocities for all unblended P Cygni lines in the optical spectrum of WRAY 16-232 (Appendix A). The velocity varies from 75 to 160 km s^{-1} in various species (Fig. 8). The H α and He I lines exhibit the highest velocities (140–160 km s^{-1}) due to their strongly blue-shifted absorption components, indicating that these transitions might be occurring in the faster moving inner regions of the envelope. In contrast, the N I, Si II, and Fe II lines show lower wind velocities of 80–120 km s^{-1}, potentially forming in denser, slower-moving layers closer to the base of the wind or within the inner regions of the layered envelope. We also computed the average

velocities for H I, He I, N I, and Fe II, which are approximately 97, 161, 86, and 105 km s^{-1}, respectively. The variation in average velocities among these different spectral species highlights the multilayered ionization structure of the WRAY 16-232 envelope. The wind–wind interactions of faster and slower winds can lead to the formation of bright arcs and knots found in *Spitzer* images (K. Weis & D. J. Bomans 2020).

3.5 Light-curve analysis of WRAY 16-232

Photometric variability, known as the S Dor cycle, is a key observational feature used to classify a star as an LBV (A. M. van Genderen 2001). Photometric studies of AG Car and S Doradus, both bona fide LBVs, have identified two distinct S Dor cycles: a shorter cycle lasting less than 10 yr and a longer cycle exceeding 20 yr (A. M. van Genderen, C. Sterken & M. de Groot 1997). Notably, no SD cycles have been observed with durations between 10 and 20 yr.

Fig. 6 presents all the light curves we plotted for WRAY 16-232. The *Gaia G*-band light curve exhibits variability of approximately 0.2–0.3 mag over its observational period, while the *ASAS-SN V*-band light curve displays a comparable level of variability during its observations. A grey vertical line indicates the date on which the spectra of WRAY 16-232 were obtained. This level of variability is consistent with the short-term fluctuations commonly observed in LBVs, likely driven by pulsational activity (H. J. G. L. M. Lamers et al. 1998), commonly observed in massive evolved stars.

We have also plotted the *Gaia BP*- and *RP*-band data (Fig. 6), which show smaller variations of about 0.1–0.2 mag, suggesting that the star was relatively stable during this time and not undergoing significant colour changes. The *Gaia BP–RP* colour index remains essentially constant during the time of observation, with a mean of 5.34 mag and a standard deviation of 0.09. This value corresponds to a very reddened object, supporting the high A_V reported for the star. The *r*-band and *i*-band light curves from M. Hackstein et al. (2015) exhibit larger variations of approximately 0.5–0.6 mag. This order of variability has also been observed in other Galactic LBVs, such as AG Car, where short S Dor (S-SD) cycles are superimposed on the long S Dor (L-SD) cycle (A. M. van Genderen 2001). This reinforces the presence of photometric variability in WRAY 16-232, and its similarities to AG Car further support its classification as an LBV.

The bottom panel of the Fig. 6 shows a combined light curve including *r*-band, *Gaia G*-band, and *ASAS-SN* V-band data. To enable a visual comparison of variability across different bands, the *ASAS-SN* data have been offset by 3.7 mag and the *r*-band data by 2.2 mag, aligning them with the *Gaia* photometry. This allows for a cohesive plot spanning from 2011 to 2018. A clear similarity in variability trends is observed in the *Gaia G*-band and *ASAS-SN* V-band data, particularly between January 2016 and July 2017, where both light curves show a notable increase in brightness.

We were unable to find long-term photometric observations of WRAY 16-232 that would capture a full L-SD phase, which limits our ability to definitively confirm its status as a LBV. We acknowledge that the variability time-scales observed in our analysis are insufficient for a conclusive classification. None the less, the presence of S-SD phase-like variability, coupled with the spectral characteristics discussed in Section 3.4, provides strong supporting evidence for its classification as an LBV. Regular monitoring of the spectroscopic variability coupled with photometry will help understand the evolution of the star and track possible beginning of S Dor phase.

3.6 Short term H α variations

We analysed at the variation of H α in the seven epochs of SALT observation. The spectra reveal short-term variability in the H α line profile (Fig. 7). The morphological changes are clearly evident in the emission peak intensities and in the shape of the wings, suggesting fluctuations on time-scales of months to years.

Line velocities, v_∞, and EW values are measured for all seven epochs and are summarized in Table 2. The H α line velocities remain nearly constant across epochs, with a variability of only ∼4 per cent. In contrast, both the EW (variability ∼22 per cent) and v_∞ (variability ∼17 per cent) show significant changes. The terminal velocities, display a clear grouping: in 2021 they cluster around ∼280 km s^{-1}, while in 2016, 2019, and 2022 they remain closer to ∼250 km s^{-1}. Such shifts in v_∞ can be linked to variations in the stellar mass-loss rate. In LBVs, it is well established that visual maximum phases, associated with enhanced mass-loss, show reduced terminal velocities, whereas in visual minimum they resemble those of normal supergiants (J. H. Groh et al. 2009). The observed differences therefore suggest higher mass-loss episodes during the 2016, 2019, and 2022 epochs compared to 2021.

4 DISCUSSION

4.1 WRAY 16-232: a promising LBV candidate

The *Spitzer* IRAC 4 image (Fig. 1) reveals a complex arc-like morphology in the nebula surrounding WRAY 16-232, likely formed by the interaction between faster winds from recent mass-loss events and slower, previously ejected material. The mid-IR *Spitzer* spectra show forbidden lines of [Fe II], [Ne III], and [S III], closely resembling those of other LBVs known to harbour dust in their environments, such as HR Car (G. Umana et al. 2009) and HD 168625 (G. Umana et al. 2010). Additionally, the presence of P Cygni profiles in H I, He I, and Fe II lines in the optical spectrum, along with a nitrogen-rich nebula indicated by numerous N I lines, further supports its classification as a LBV candidate.

4.2 Implications of fullerene detection

A detailed examination of the central, north and south spectral regions, as shown in Fig. 2, reveals that the central region is devoid of PAHs and C_{60}. The illuminated regions in the IR images appear denser and brighter than their surroundings. It is possible that these clumpy regions are partially shielded from intense UV radiation, giving ideal conditions of complex molecules to form, while still receiving enough exposure to facilitate their excitation. This distinct environment may have contributed to the formation of (i) PAHs through a bottom-up process facilitated by hydrogen-rich conditions, and subsequently (ii) C_{60} through shock-induced top-down fragmentation of larger PAHs observed in the ejecta during the LBV phase (see Sections 4.2.1 and 4.2.2 for further discussion).

A potential pathway for fullerene formation is suggested in the theoretical work of E. R. Micelotta, A. P. Jones & A. G. G. M. Tielens (2010a) and E. R. Micelotta, A. P. Jones & A. G. G. M. Tielens (2010b), which proposes that PAHs could transform into C_{60} through shock-driven processes. Their studies indicate that shock velocities of 75–150 km s^{-1} can significantly modify the structure of PAHs, a velocity range comparable to the slow winds of LBVs. Fig. 8 presents a velocity box plot of the various species identified in the optical spectrum of WRAY 16-232. Transitions associated with

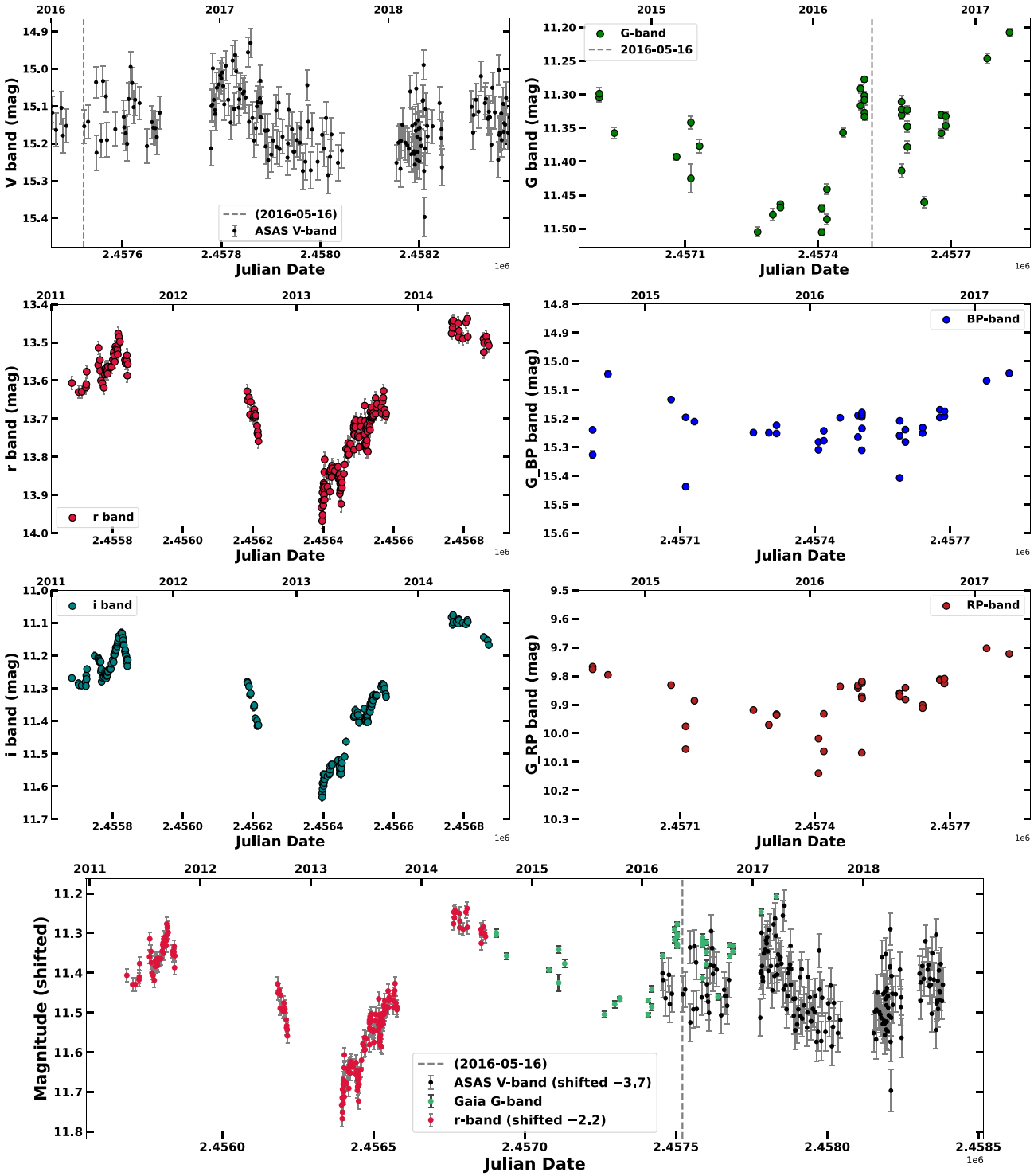

Figure 6. Multiband photometric variability of WRAY 16-232 from different surveys and filters. Top row: Left panel shows the *ASAS-SN V*-band light curve from 2016 to 2018; right panel shows the *Gaia G*-band light curve from 2015 to 2017. Middle row: Left panel displays *r*-band magnitudes; right panel shows *Gaia BP* magnitudes from 2015 to 2017. Third row: Left panel presents *i*-band magnitudes; right panel shows *Gaia RP* magnitudes. Bottom panel: Combined light curve showing *r*-band (*r*-band offset by −2.2 mag), *V*-band (*ASAS-SN*, offset by −3.7 mag) and *Gaia G*-band photometry, with magnitudes shifted for visual comparison. The vertical dashed line marks the epoch when the spectrum was obtained.

nitrogen, silicon, hydrogen (Paschen series), and iron predominantly fall within the low-velocity range of 75–100 km s^{-1}, whereas a higher-velocity range of 120–170 km s^{-1} is associated with He I and Hα. Shock regions and shielded dense regions can be created by wind–wind interactions in the shells of LBVs (K. Weis & D. J. Bomans 2020). This suggests that, in the stellar envelope of WRAY 16-232, there may be regions where the velocity conditions facilitate the processing of PAHs into C_{60}.

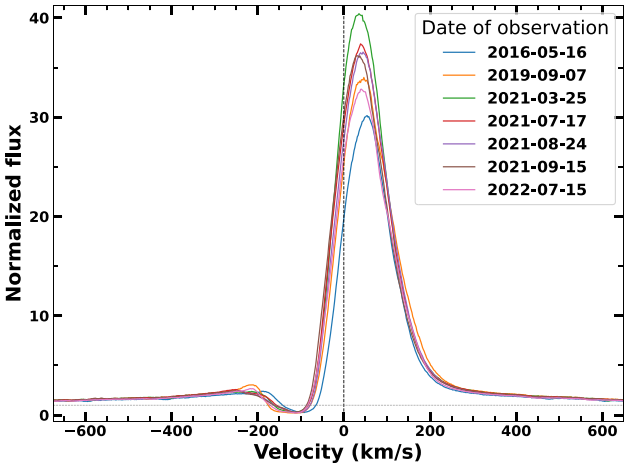

Figure 7. Multi-epoch SALT spectra of WRAY 16-232 plotted on the velocity scale relative to the rest wavelength of H α (6562.8 Å dashed line). Each epoch is shown in a different colour for clarity, and short-term variability in the H α line is clearly evident over the course of the observations.

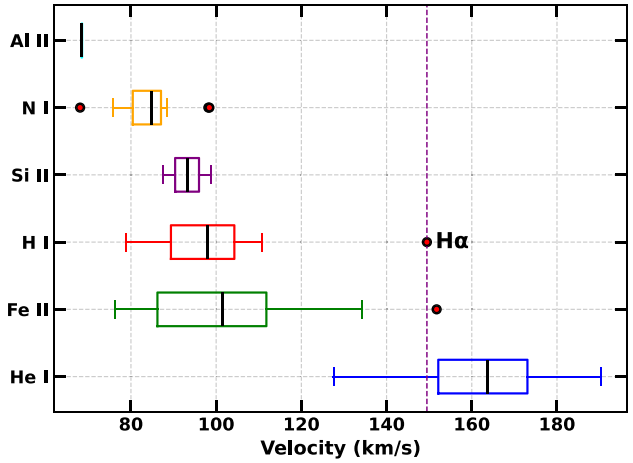

Figure 8. Box plot of the species identified in the optical spectrum of WRAY 16-232. Outliers for each species are indicated by red circles. The line within each box represents the median velocity, below which 50 per cent of the transitions for that species are found.

Table 2. Summary of H α measurements at different epochs. Line velocities are reported with 3σ errors and EW values are given with 1σ standard deviations.

Epoch	Line velocity (km s^{-1})	v_∞ (km s^{-1})	EW (Å)
2016-05-16	150.00 ± 1.11	244	−27.79 ± 1.63
2019-09-07	151.20 ± 1.31	253	−30.01 ± 2.08
2021-03-25	149.04 ± 0.97	249	−34.67 ± 1.78
2021-07-17	151.29 ± 1.01	289	−31.54 ± 1.74
2021-08-24	149.26 ± 1.09	283	−30.95 ± 1.73
2021-09-15	145.31 ± 1.02	279	−30.88 ± 1.44
2022-07-22	151.22 ± 1.24	255	−29.22 ± 0.98

To our knowledge, the theoretical work by E. R. Micelotta et al. (2010a), E. R. Micelotta et al. (2010b) has never been tested observationally. WRAY 16-232 and its shell may provide a testing ground to observationally verify fullerene formation through shocks. Furthermore, this could indicate that such PAH-to-fullerene transformation occurs specifically in more LBV-type environments. Here, we explore the physical and temporal constrains of this possible process.

4.2.1 *Physical constraints on fullerene survival*

First, we estimate the UV radiation field strength (G_0) and compare it to known survival thresholds for fullerenes. Fullerenes like C_{60} are resilient in moderate UV environments but undergo photodissociation in intense fields, typically surviving in $G_0 < 10^4$–10^5 Habing units (H. J. Habing 1968; O. Berné & A. G. G. M. Tielens 2012; O. Berné et al. 2015). In PN and RNe where C_{60} is commonly detected, G_0 ranges from 10^2 to 10^5 Habing units, with higher values requiring additional shielding from gas or dust to prevent destruction (K. Sellgren et al. 2010). G_0 values in LBVs get significantly reduced with distance and attenuation by dust clumps or shells.

We calculate G_0 at the observed shell radius ($r_{\rm shell} \approx 0.7$ pc). For LBV candidates like WRAY 16-232, which exhibit spectral features consistent with a quiescent phase (e.g. $T_{\rm eff} \sim 12\,000$–$30\,000$ K) from the absence of higher ionization lines and presence of Fe II $L_{\rm bol}$ typically ranges from 10^5 to 10^6 $L_\odot$ (R. M. Humphreys & K. Davidson 1994). This puts our estimates of G_0 approximately in the range of 10^3–10^4 Habing units, which fall within the survival regime for C_{60}, particularly in the outer shell where UV dilution is significant. However, near the central star, G_0 could exceed 10^5 Habing units, potentially leading to rapid photodissociation. It matches with the central region spectra which does not show Carbon compounds. Survival thus requires attenuation, consistent with the high extinction ($A_V \approx 12$ mag) and clumpy morphology observed in the IRAC 8 μm image (Fig. 1), which suggests the presence of dense regions ($n_{\rm H} > 10^4$ cm^{-3}) providing shielding.

The presence of the 16.4 μm PAH feature in the envelope spectra (Fig. 3) further informs the chemical environment and formation pathway. This band is attributed to large PAHs with $N_{\rm C} \gtrsim 50$–130 (C. Boersma et al. 2010), indicating a carbon- and hydrogen-rich ejecta typical of LBVs undergoing CNO-processed mass-loss but retaining sufficient H for PAH formation (J. S. Vink 2018a). In such environments, C_{60} likely forms via a 'top–down' process, where these large PAHs are dissociated into smaller fragments (e.g. graphenes or C_n chains) by UV photons or shocks, subsequently isomerizing into cage structures (J. Bernard-Salas et al. 2012; A. Omont & H. F. Bettinger 2021). This hydrogen rich ejecta makes it less efficient to form 'bottom-up' formation of C_{60}. The estimated $G_0 \sim 10^3$–10^4 Habing units is sufficient for photodissociation of PAHs (threshold $G_0 > 10^3$ Habing units; E. R. Micelotta et al. 2010a) without complete destruction, supporting this mechanism. Alternatively, wind-driven shocks (velocities 75–170 km s^{-1}) could enhance dissociation, as modelled by E. R. Micelotta et al. (2010a), where $v_{\rm shock} \sim 100$ km s^{-1} yields destruction efficiencies of $\eta \sim 0.1$–1 per cent per event, allowing gradual processing over multiple episodes.

4.2.2 *Time-scales for top–down C_{60} formation*

We found that the photodissociation and shock formations are possible in the environment of WRAY 16-232. To evaluate the feasibility of these top–down C_{60} formation, we estimate the time-scales for two competing mechanisms, UV photodissociation and, shock/wind processing and compare them to the LBV phase duration

($\sim 10^4$–10^5 yr; R. M. Humphreys 1991). We estimate the shell expansion time-scale to be ≈ 7000 yr, considering wind velocity of 100 kms^{-1} with a shell radius of 0.7 pc.

In RNe like NGC 7023, top–down formation occurs via UV photodissociation of large PAHs ($N_C \gtrsim 50$–130), involving sequential H-loss and C_2 ejection. This requires multiple photon absorptions to overcome high activation energies ($\sim$ 10–15 eV per C_2 loss). Models indicate a time-scale of $\sim 10^5$ yr for complete conversion (e.g. $C_{66}H_{20}$ to C_{60}) in regions with $G_0 \sim 10^3$–10^4 Habing units (O. Berné & A. G. G. M. Tielens 2012), which exceeds the LBV phase duration. The mechanism of photodissociaton is too slow to produce observable amount of C_{60} within the LBV phase.

On the contrary, shock processing in LBVs, driven by wind–wind interaction provides a faster pathway. These shocks recur on S Dor cycles (10–20 yr), within total LBV time-scales of $\sim 10^3$–10^5 yr. The destruction efficiency of PAHs in shocks is $\sim$ 20–40 per cent C-loss per event for 75–100 km s^{-1} shocks (E. R. Micelotta et al. 2010a), modelled via nuclear stopping.

For WRAY 16-232, shocks fragment large PAHs (evidenced by the 16.4 μm band) into C_{60}-like structures, with lab analogues showing rapid fullerene production from HACs (D. A. García-Hernández et al. 2010; J. Bernard-Salas et al. 2012). Cumulative processing over numerous shocks could yield observable C_{60} in $< 10^4$ yr, fitting the LBV phase and shell expansion. Thus, while UV photodissociation is too slow, shock/wind processing aligns with LBV evolution, producing C_{60} efficiently in the clumpy, carbon-rich shell of WRAY 16-232.

Our G_0 estimates predict that C_{60} is favoured in the outer, shielded shell regions, whereas it is destructed in regions close to the star. This supports shock formation from wind–wind interactions, as evidenced by the arc-like structures in the shell (Fig. 1).

To test the wind interaction model of (E. R. Micelotta et al. 2010a), high-resolution integral field spectroscopy and imaging in the near and MIR wavelengths are essential. This presents a strong case for obtaining high-resolution *James Webb Space Telescope* (*JWST*; J. P. Gardner et al. 2006) observations of WRAY 16-232, which would allow us to directly investigate the proposed C_{60} formation mechanisms, resolve G_0 gradients in the shell and could potentially target shock tracers [e.g. $H_2S(0)$-$S(3)$ lines].

This is the first ever detection of C_{60} in a LBV environment and may have huge implications on the formation of the species. Fullerenes may be forming in the ejecta during episodic mass-loss events through shocks or through bottom-up processes specific to the LBVs or other massive stellar environments. As massive stars with relatively short lifetimes, LBVs, especially WRAY 16-232, provide a unique opportunity to study the time-scales and mechanisms of C_{60} formation.

5 END REMARKS AND FUTURE WORK

The present study of WRAY 16-232 supports its previously proposed classification as a strong LBV candidate while also revealing that its circumstellar environment exhibits unique chemical signatures. Our analysis, based on *Spitzer* MIR spectra, SALT optical HRS spectra, and photometric data from *Gaia*, ASAS-SN and Bochum GDS has highlighted the existence of complex mass-loss dynamics and dust formation processes.

The results provide new insights into the interplay between stellar winds, dust formation, and molecular chemistry in LBV shells. Moreover, with the detection of C_{60} molecule in the environment of WRAY 16-232, we find observational evidence for formation pathway for C_{60} in LBV environments through shock-driven process. This discovery has implication to carbon dust formation in the outer shells of massive stars.

Further investigations involving long-term multi-epoch high-resolution spectroscopy and high cadence photometry would help in investigating a complete S-Dor cycle of WRAY 16-232. Given its carbonaceous molecular complexity and expanding stellar winds, WRAY 16-232 emerges as an ideal candidate for future high-resolution observations using *JWST*.

ACKNOWLEDGEMENTS

The authors thank the referee for the meticulous review. SAP thanks the BGS, Director and Dean Indian Institute of Astrophysics (IIA), for providing the opportunity to work under the Visiting Student Program (VSP) at IIA. BM acknowledges the financial support by the SERB project (CRG/2023/005271). Some of the observations reported in this paper were obtained with the SALT under programme [2016-1-SCI-012 – PI:Alexei Kniazev]. This work has made use of data from the European Space Agency (ESA) mission *Gaia* (https://www.cosmos.esa.int/gaia), processed by the *Gaia* Data Processing and Analysis Consortium (DPAC; https://www.cosmos.esa.int/web/gaia/dpac/consortium). Funding for the DPAC has been provided by national institutions, in particular the institutions participating in the *Gaia* Multilateral Agreement. Also, ChatGPT (OpenAI 2023) is used for assistance in correcting typos and grammar, though full responsibility for the manuscript's content remains our own.

DATA AVAILABILITY

The *Spitzer* IRS data from the CASSIS can be accessed at https://cassis.sirtf.com/ and CASSISJuice.[4] The complete results produced by this study will be made available to interested parties upon request to the corresponding author

REFERENCES

Acker A., Marcout J., Ochsenbein F., Stenholm B., Tylenda R., Schohn C., 1992, The Strasbourg-ESO Catalogue of Galactic Planetary Nebulae. Parts I, II. European Southern Observatory, Garching
Allen D. A., Baines D. W. T., Blades J. C., Whittet D. C. B., 1982, MNRAS, 199, 1017
Arun R. et al., 2021, MNRAS, 507, 267
Arun R., Mathew B., Manoj P., Maheswar G., Shridharan B., Kartha S. S., Narang M., 2023, MNRAS, 523, 1601
Banerjee G. et al., 2022, J. Astrophys. Astron., 43, 102
Barnes S. I. et al., 2008, in McLean I. S., Casali M. M., eds, Proc. SPIE Conf. Ser. Vol. 7014, Ground-based and Airborne Instrumentation for Astronomy II. SPIE, Bellingham, p. 70140K
Benjamin R. A. et al., 2003, PASP, 115, 953
Bernard-Salas J., Cami J., Peeters E., Jones A. P., Micelotta E. R., Groenewegen M. A. T., 2012, ApJ, 757, 41
Bernat A. P., Lambert D. L., 1978, PASP, 90, 520
Berné O., Tielens A. G. G. M., 2012, Proc. Natl. Acad. Sci., 109, 401
Berné O., Montillaud J., Joblin C., 2015, A&A, 577, A133
Boersma C., Bauschlicher C. W., Allamandola L. J., Ricca A., Peeters E., Tielens A. G. G. M., 2010, A&A, 511, A32
Bouchy F., Pepe F., Queloz D., 2001, A&A, 374, 733

[4]https://gitlab.com/cassisjuice

Bramall D. G. et al., 2010, in McLean I. S., Ramsay S. K., Takami H., eds, Proc. SPIE Conf. Ser. Vol. 7735, Ground-based and Airborne Instrumentation for Astronomy III. SPIE, Bellingham, p. 77354F
Bramall D. G. et al., 2012, in McLean I. S., Ramsay S. K., Takami H., eds, Proc. SPIE Conf. Ser. Vol. 8446, Ground-based and Airborne Instrumentation for Astronomy IV. SPIE, Bellingham, p. 84460A
Cami J., Bernard-Salas J., Peeters E., Malek S. E., 2010, Science, 329, 1180
Carey S. J. et al., 2009, PASP, 121, 76
Carvalho A. S., Hillenbrand L. A., 2022, ApJ, 940, 156
Chmielewski Y., 2000, A&A, 353, 666
Clark J. S., Castro N., Garcia M., Herrero A., Najarro F., Negueruela I., Ritchie B. W., Smith K. T., 2012, A&A, 541, A146
Crause L. A. et al., 2014, in Ramsay S. K., McLean I. S., Takami H., eds, Proc. SPIE Conf. Ser. Vol. 9147, Ground-based and Airborne Instrumentation for Astronomy V. SPIE, Bellingham, p. 91476T
Crawford S. M. et al., 2010, in Silva D. R., Peck A. B., Soifer B. T., eds, Proc. SPIE Conf. Ser. Vol. 7737, Observatory Operations: Strategies, Processes, and Systems III. SPIE, Bellingham, p. 773725
Crichton R. A., Zhang J., 2022, in Lu X., Akasaka T., Slanina Z., eds, Formation Mechanism of Fullerenes/Metallofullerenes. Springer Nature Singapore, Singapore, p. 991 https://doi.org/10.1007/978-981-16-8994-9_44
Davidson K., Walborn N. R., Gull T. R., 1982, ApJ, 254, L47
Deharveng L. et al., 2010, A&A, 523, A6
Fazio G. G. et al., 2004, ApJS, 154, 10
Friedman S. D. et al., 2010, ApJ, 727, 33
Gaia Collaboration, 2016, A&A, 595, A1
Gaia Collaboration, 2023, A&A, 674, A1
García-Hernández D. A., Manchado A., García-Lario P., Stanghellini L., Villaver E., Shaw R. A., Szczerba R., Perea-Calderón J. V., 2010, ApJ, 724, L39
García-Hernández D. A., Kameswara Rao N., Lambert D. L., 2011, ApJ, 729, 126
García-Hernández D. A., Villaver E., García-Lario P., Acosta-Pulido J. A., Manchado A., Stanghellini L., Shaw R. A., Cataldo F., 2012, ApJ, 760, 107
Gardner J. P. et al., 2006, Space Sci. Rev., 123, 485
Groh J. H., Hillier D. J., Damineli A., Whitelock P. A., Marang F., Rossi C., 2009, ApJ, 698, 1698
Groh J. H., Meynet G., Ekström S., 2013, A&A, 550, L7
Groh J. H., Meynet G., Ekström S., Georgy C., 2014, A&A, 564, A30
Gvaramadze V. V., Kniazev A. Y., Fabrika S., 2010, MNRAS, 405, 1047
Habing H. J., 1968, Bull. Astron. Inst. Netherlands, 19, 421
Hackstein M. et al., 2015, Astron. Nachr., 336, 590
Henize K. G., 1967, ApJS, 14, 125
Humphreys R. M., 1991, in van der Hucht K. A., Hidayat B., eds, IAU Symposium, Vol. 143, Wolf-Rayet Stars and Interrelations with Other Massive Stars in Galaxies. Kluwer, Dordrecht, p. 485
Humphreys R. M., Davidson K., 1994, PASP, 106, 1025
Humphreys R. M., Weis K., Davidson K., Bomans D. J., Burggraf B., 2014, ApJ, 790, 48
Irle S., Wang Z., Zheng G., Morokuma K., Kusunoki M., 2006, J. Chem. Phys., 125, 044702
Jayasinghe T. et al., 2019, MNRAS, 468, 1907
Jenniskens P., Desert F. X., 1994, A&AS, 106, 39
Jiménez-Esteban F. M., Rizzo J. R., Palau A., 2010, ApJ, 713, 429
Johnson R. D., Meijer G., Bethune D. S., 1990, J. Am. Chem. Soc., 112, 8983
Klochkova V. G., Islentieva E. S., Panchuk V. E., 2022, Astron. Rep., 66, 998
Kniazev A. Y., Gvaramadze V. V., Berdnikov L. N., 2016, MNRAS, 459, 3068–3077
Kniazev A. Y., Gvaramadze V. V., Berdnikov L. N., 2017, in Balega Y. Y., Kudryavtsev D. O., Romanyuk I. I., Yakunin I. A., eds, ASP Conf. Ser. Vol. 510, Stars: From Collapse to Collapse. Astron. Soc. Pac., San Francisco, p. 480
Kochanek C. S. et al., 2017, PASP, 129, 104502
Kogure T., Leung K.-C., 2007, The Astrophysics of Emission-Line Stars, Astrophysics and Space Science Library, Vol. 342. Springer-Verlag, New York.
Kramida A., Yu. Ralchenko, Reader J., and NIST ASD Team, 2024, NIST Atomic Spectra Database (ver. 5.12), [Online]. Available: https://physics.nist.gov/asd (accessed 2025 January 21). National Institute of Standards and Technology, Gaithersburg, MD
Kroto H. W., Heath J. R., Obrien S. C., Curl R. F., Smalley R. E., 1985, Nature, 318, 162
Lamers H. J. G. L. M., Korevaar P., Cassatella A., 1985, A&A, 149, 29
Lamers H. J. G. L. M., Bastiaanse M. V., Aerts C., Spoon H. W. W., 1998, A&A, 335, 605
Lebouteiller V., 2023, preprint (arXiv:2309.06876)
Lebouteiller V., Barry D. J., Spoon H. W. W., Bernard-Salas J., Sloan G. C., Houck J. R., Weedman D. W., 2011, ApJS, 196, 8
Lebouteiller V., Barry D. J., Goes C., Sloan G. C., Spoon H. W. W., Weedman D. W., Bernard-Salas J., Houck J. R., 2015, ApJS, 218, 21
MacConnell D. J., 1983, RMxAA, 8, 39
Mahy L., Hutsemékers D., Royer P., Waelkens C., 2016, A&A, 594, A94
Mahy L. et al., 2022, A&A, 657, A4
Ma X.-X. et al., 2024, A&A, 691, A282
Marchenko S. V., Moffat A. F. J., 2017, MNRAS, 468, 2416
Marcolino W. L. F., Bouret J. C., Lanz T., Maia D. S., Audard M., 2017, MNRAS, 470, 2710
Massey P., Waterhouse E., DeGioia-Eastwood K., 2000, AJ, 119, 2214
Mehner A. et al., 2021, A&A, 655, A33
Micelotta E. R., Jones A. P., Tielens A. G. G. M., 2010a, A&A, 510, A36
Micelotta E. R., Jones A. P., Tielens A. G. G. M., 2010b, A&A, 510, A37
Micelotta E. R., Jones A. P., Cami J., Peeters E., Bernard-Salas J., Fanchini G., 2012, ApJ, 761, 35
Morris P., Morris P. W., WRRINGS Team Spitzer , 2008, in Bresolin F., Crowther P. A., Puls J., eds, IAU Symposium, Vol. 250, Massive Stars as Cosmic Engines. Cambridge Univ. Press , Cambridge, p. 361
Najarro F., Hillier D. J., Stahl O., 1997, A&A, 326, 1117
Nidhi S., Mathew B., Shridharan B., Arun R., Anusha R., Kartha S. S., 2023, MNRAS, 524, 5166
Nota A., 1999, in Wolf B., Stahl O., Fullerton A. W., eds, IAU Colloq. 169: Variable and Non-spherical Stellar Winds in Luminous Hot Stars, Vol. 523. Springer-Verlag, New York, p. 62
Nowak M., Flagey N., Noriega-Crespo A., Billot N., Carey S. J., Paladini R., Van Dyk S. D., 2014, ApJ, 796, 116
Omont A., Bettinger H. F., 2021, A&A, 650, A193
Otsuka M., Kemper F., Cami J., Peeters E., Bernard-Salas J., 2013, MNRAS, 437, 2577
Puls J., Vink J. S., Najarro F., 2008, A&AR, 16, 209
Rajagopal J. et al., 2007, ApJ, 671, 2017
Raman V. V., Anandarao B. G., Janardhan P., Pandey R., 2017, MNRAS, 470, 1593
Richardson N. D., Mehner A., 2018, Res. Notes Am. Astron. Soc., 2, 121
Rieke G. H. et al., 2004, ApJS, 154, 25
Rivinius T., Carciofi A. C., Martayan C., 2013, A&AR, 21, 69
Rizzo J. R. et al., 2023, A&A, 678, A55
Roberts K. R. G., Smith K. T., Sarre P. J., 2012, MNRAS, 421, 3277
Rottenberg J. A., 1952, MNRAS, 112, 125
Sanduleak N., Stephenson C. B., 1973, ApJ, 185, 899
Sellgren K., Werner M. W., Ingalls J. G., Smith J. D. T., Carleton T. M., Joblin C., 2010, ApJ, 722, L54–L57
Seok J. Y., Li A., 2017, ApJ, 835, 291
Shappee B. J. et al., 2014, ApJ, 788, 48
Skinner C. J., 1997, in Nota A., Lamers H., eds, ASP Conf. Ser. Vol. 120, Luminous Blue Variables: Massive Stars in Transition. Astron. Soc. Pac., San Francisco, p. 322
Słyk K., Galazutdinov G. A., Musaev F. A., Bondar A. V., Schmidt M. R., Krełowski J., 2006, A&A, 448, 221
Smith N., Aghakhanloo M., Murphy J. W., Drout M. R., Stassun K. G., Groh J. H., 2019, MNRAS, 488, 1760
Stahl O., Mandel H., Szeifert T., Wolf B., Zhao F., 1991, A&A, 244, 467

Stahl O., Jankovics I., Kovács J., Wolf B., Schmutz W., Kaufer A., Rivinius T., Szeifert T., 2001, A&A, 375, 54
Umana G., Buemi C. S., Trigilio C., Hora J. L., Fazio G. G., Leto P., 2009, ApJ, 694, 697
Umana G., Buemi C. S., Trigilio C., Leto P., Hora J. L., 2010, ApJ, 718, 1036
van Genderen A. M., 2001, A&A, 366, 508
van Genderen A. M., Sterken C., de Groot M., 1997, A&A, 318, 81
Vink J. S., 2008, New Astron. Rev., 52, 419
Vink J. S., 2018a, A&A, 615, A119
Vink J. S., 2018b, A&A, 619, A54
Voors R. H. M., Waters L. B. F. M., Morris P. W., Trams N. R., de Koter A., Bouwman J., 1999, A&A, 341, L67
Voors R. H. M. et al., 2000, A&A, 356, 501
Webster L. B., 1966, PASP, 78, 136
Weis K., Bomans D. J., 2020, Galaxies, 8, 20
Weis K., Duschl W. J., Bomans D. J., 2003, A&A, 398, 1041
Wray J. D., 1966, PhD thesis, Northwestern University
Wu K.-F., Luo A. L., Chen J.-J., Hou W., Zhao Y.-H., 2022, Res. Astron. Astrophys., 22, 085007

APPENDIX A: DETECTED LINES

We present the detected spectral lines with their observed and laboratory wavelengths, noting whether they show P Cygni profiles in Table A1. Line identifications follow A. Kramida et al. (2024). For P Cygni lines that are clearly resolved and unblended, we also provide accurate terminal velocity measurements. Velocity uncertainties were estimated from the photon-noise limit, following F. Bouchy, F. Pepe & D. Queloz (2001). For a given wavelength region, we measured the local continuum signal-to-noise ratio (S/N) and used it to compute the velocity error as $\sigma_v = \frac{c/R}{\mathrm{S/N}}$, where c is the speed of light and R is the resolving power of SALT HRS ($\approx 14{,}000$ in low-resolution mode). Each measured S/N value was then applied to all spectral lines within the corresponding wavelength interval. This procedure yields the minimum statistical error expected for our spectra. We report three times this value ($3\sigma_v$) as the velocity error.

Table A1. Identified spectral lines in the optical spectrum of WRAY 16-232 within the wavelength range of 5500–8800 Å. Column 1 indicates the species, Column 2 shows the observed wavelength in the spectrum, and Column 3 provides the corresponding laboratory wavelength (in air) from A. Kramida et al. (2024). Column 4 specifies whether the line exhibits a P Cygni profile, and Column 5 presents the velocity measured for the clearly distinguishable P Cygni lines.

Species	Observed wavelength (Å)	Laboratory wavelength (Å, air)	P Cygni profile	Velocity (km s^{-1})
Fe II	5535.00	5534.89	Yes	
[Fe II]	5747.48	5746.97	No	
[N II]	5754.48	5754.59	No	
Fe II	5813.58	5813.66	Yes	92 ± 4.95
Fe II	5835.28	5835.45	Yes	
He I	5876.66	5877.25	Yes	190 ± 4.95
Fe II	5952.70	5952.51	Yes	106 ± 4.95
Si II	5957.90	5957.56	No	
Si II	5979.04	5978.93	No	
Fe II	5991.26	5991.37	Yes	
[Fe II]	6045.06	6044.10	No	
Fe II	6084.24	6084.10	Yes	
Fe II	6103.22	6103.90	Yes	98 ± 4.95
Fe II	6149.06	6149.23	Yes	152 ± 4.95
Fe II	6179.46	6179.37	Yes	104 ± 4.95
Fe II	6238.95	6238.37	Yes	127 ± 1.62
Fe II	6247.60	6247.55	Yes	111 ± 1.62
Fe II	6305.21	6305.29	Yes	99 ± 1.62
Fe II	6317.93	6318.01	No	
Fe II	6331.92	6331.95	Yes	82 ± 1.62
Si II	6347.29	6347.10	Yes	99 ± 1.62
Si II	6371.60	6371.36	Yes	88 ± 1.62
Fe II	6383.82	6383.72	Yes	
Fe II	6385.78	6385.45	–	
Fe II	6416.92	6416.93	Yes	89 ± 1.62
Fe II	6432.66	6432.67	Yes	112 ± 1.62
Fe II	6456.39	6456.38	Yes	134 ± 1.62
N II	6482.28	6482.05	Yes	87 ± 1.62
Fe II	6491.26	6491.25	–	
Fe II	6492.79	6493.04	–	
Fe II	6515.87	6516.07	Yes	
Fe II	6516.85	6517.02	Yes	
Hα	6563.45	6562.79	Yes	150 ± 1.11
C II	6582.96	6582.87	No	
[N II]	6582.96	6583.45	No	
Fe II	6626.94	6627.23	Yes	81 ± 1.11
He I	6678.93	6679.99	Yes	160 ± 1.05
[S II]	6717.19	6716.44	No	
Al II	6823.56	6823.48	No	
N II	6966.86	6966.81	Yes	98 ± 0.48
Al II	7042.29	7042.06	Yes	69 ± 0.48
Al II	7056.66	7056.60	Yes	68 ± 0.48
He I	7065.77	7065.19	Yes	167 ± 0.48
Fe II	7134.77	7134.54	Yes	85 ± 0.48
[Fe II]	7155.23	7155.17	No	
Fe II	7222.21	7222.39	Yes	93 ± 0.42
Fe II	7320.49	7320.70	Yes	80 ± 0.42
N I	7423.91	7423.64	Yes	84 ± 0.42
N I	7442.38	7442.29	Yes	80 ± 0.42
Fe II	7449.42	7449.34	Yes	98 ± 0.42
Fe II	7462.39	7462.41	Yes	109 ± 0.42
N I	7468.89	7468.31	Yes	98 ± 0.42
Fe II	7479.58	7479.70	Yes	76 ± 0.42
Fe II	7494.94	7494.69	No	
Fe II	7495.69	7495.62	No	
Fe II	7506.62	7506.54	–	
Fe II	7513.33	7513.17	No	
Fe II	7515.15	7515.10	No	
Fe II	7533.34	7532.50	Yes	109 ± 0.42

Table A1 – *continued*

Species	Observed wavelength (Å)	Laboratory wavelength (Å, air)	P Cygni profile	Velocity (km s^{-1})
Fe II	7711.60	7711.43	Yes	113 ± 0.45
Fe II	7731.68	7731.68	No	
Fe II	7755.63	7756.00	No	
O I	7772.11	7771.94	–	
O I	7775.67	7775.39	Yes	
Fe II	7789.13	7789.27	No	
Fe II	7801.27	7801.19	No	
Fe II	7818.16	7818.32	No	
Si II	7848.94	7849.72	No	
Si II	7849.52	7848.80	No	
Fe II	7866.54	7866.55	No	
Mg II	7877.06	7877.05	No	
Mg II	7896.49	7896.36	No	
Fe II	7917.86	7917.79	No	
Fe II	7975.85	7975.91	No	
Fe II	7981.77	7981.91	No	
H I (P35)	8264.57	8264.28	Yes	
H I (P29)	8292.61	8292.30	Yes	
H I (P28)	8298.41	8298.83	Yes	
H I (P27)	8306.15	8306.10	Yes	
H I (P26)	8314.60	8314.26	Yes	
H I (P25)	8324.34	8323.42	Yes	105 ± 0.24
H I (P24)	8334.07	8333.78	Yes	
H I (P23)	8345.75	8345.54	Yes	88 ± 0.24
H I (P22)	8359.13	8359.00	Yes	79 ± 0.24
H I (P21)	8375.07	8374.48	Yes	102 ± 0.24
H I (P20)	8392.76	8392.40	Yes	100 ± 0.24
H I (P19)	8413.68	8413.32	Yes	92 ± 0.24
H I (P18)	8438.11	8437.95	Yes	
O I	8446.60	8446.36	Yes	
Fe II	8450.91	8451.01	Yes	
H I (P17)	8468.47	8467.26	Yes	
Ca II	8497.92	8498.02	Yes	
H I (P16)	8502.72	8502.49	Yes	
Ca II	8542.19	8542.09	Yes	
H I (P15)	8545.43	8545.38	Yes	
N I	8567.79	8567.74	Yes	83 ± 0.24
He I	8582.95	8582.62	Yes	128 ± 0.24
H I (P14)	8598.77	8598.39	Yes	96 ± 0.24
N I	8629.30	8629.24	Yes	
Ca II	8662.18	8662.14	Yes	
H I (P13)	8665.16	8665.02	Yes	
N I	8680.24	8680.28	Yes	
N I	8683.14	8683.40	Yes	
N I	8686.33	8686.15	Yes	
N I	8703.48	8703.25	Yes	87 ± 0.24
N I	8712.01	8711.70	Yes	87 ± 0.24
N I	8719.13	8718.83	Yes	88 ± 0.24
N I	8729.03	8728.89	Yes	81 ± 0.24
H I (P12)	8751.44	8750.46	Yes	111 ± 0.24

This paper has been typeset from a TEX/LATEX file prepared by the author.